The Unluckiest Star: A Spectroscopically Confirmed Repeated Partial Tidal Disruption Event AT 2022dbl

Zheyu Lin[1,2] , Ning Jiang[1,2] , Tinggui Wang[1,2,3] , Xu Kong[1,2,3] , Dongyue Li[4] , Han He[5] , Yibo Wang[1,2] ,
Jiazheng Zhu[1,2] , Wentao Li[1,2] , Ji-an Jiang[1,2,6] , Avinash Singh[7] , Rishabh Singh Teja[8,9] , D. K. Sahu[8] ,
Chichuan Jin[4] , Keiichi Maeda[10] , and Shifeng Huang[1,2]

[1] Department of Astronomy, University of Science and Technology, Hefei 230026, People's Republic of China; linzheyu@mail.ustc.edu.cn, jnac@ustc.edu.cn,
twang@ustc.edu.cn, xkong@ustc.edu.cn
[2] School of Astronomy and Space Sciences, University of Science and Technology of China, Hefei 230026, People's Republic of China
[3] Institute of Deep Space Sciences, Deep Space Exploration Laboratory, Hefei 230026, People's Republic of China
[4] National Astronomical Observatories, Chinese Academy of Sciences, Beijing 100101, People's Republic of China
[5] Department of Astronomy, School of Physics and Technology, Wuhan University, Wuhan 430072, People's Republic of China
[6] National Astronomical Observatory of Japan, 2-21-1 Osawa, Mitaka, Tokyo 181-8588, Japan
[7] Hiroshima Astrophysical Science Center, Hiroshima University, Higashi-Hiroshima, Hiroshima 739-8526, Japan
[8] Indian Institute of Astrophysics, II Block, Koramangala, Bengaluru-560034, Karnataka, India
[9] Pondicherry University, R.V. Nagar, Kalapet, Pondicherry-605014, UT of Puducherry, India
[10] Department of Astronomy, Kyoto University, Kitashirakawa-Oiwake-cho, Sakyo-ku, Kyoto 606-8502, Japan

Abstract

The unluckiest star orbits a supermassive black hole elliptically. Every time it reaches the pericenter, it shallowly enters the tidal radius and gets partially tidally disrupted, producing a series of flares. Confirmation of a repeated partial tidal disruption event (pTDE) requires not only evidence to rule out other types of transients but also proof that only one star is involved, as TDEs from multiple stars can also produce similar flares. In this Letter, we report the discovery of a repeated pTDE, AT 2022dbl. In a quiescent galaxy at $z = 0.0284$, two separate optical/UV flares have been observed in 2022 and 2024 with no bright X-ray, radio, or mid-infrared counterparts. Compared to the first flare, the second flare has a similar blackbody temperature of $\sim$26,000 K, slightly lower peak luminosity, and slower rise and fall phases. Compared to the Zwicky Transient Facility TDEs, their blackbody parameters and light-curve shapes are all similar. The spectra taken during the second flare show a steeper continuum than the late-time spectra of the previous flare, consistent with a newly risen flare. More importantly, the possibility of two independent TDEs can be largely ruled out because the optical spectra taken around the peak of the two flares exhibit highly similar broad Balmer, N III, and possible He II emission lines, especially the extreme $\sim$4100 Å emission lines. This represents the first robust spectroscopic evidence for a repeated pTDE, which can soon be verified by observing the third flare, given its short orbital period.

1. Introduction

An unlucky star passes too close to a supermassive black hole (SMBH). It gets tidally torn apart and produces a luminous flare. In this case, a tidal disruption event (TDE) occurs (Hills 1975; Rees 1988). The discovery of these TDEs has been limited by the relatively low occurrence rate of about 10^{-4}–10^{-5} galaxy^{-1} yr^{-1} (e.g., Wang & Merritt 2004; Stone & Metzger 2016; van Velzen et al. 2020; Yao et al. 2023; Teboul et al. 2024). From the late 1990s to the late 2000s, only $\sim$10 TDEs had been discovered. Most of them are bright in the X-ray bands (e.g., Bade et al. 1996; Komossa & Bade 1999; Esquej et al. 2007), which is in concordance with the early theoretical prediction that the emission peaks in the extreme-UV to soft X-ray bands (e.g., Cannizzo et al. 1990; Rees 1990; Ulmer 1999). In the last decade, however, more TDEs have been discovered by wide-field optical surveys, such as the All-Sky Automated Survey for Supernovae (ASAS-SN), the Asteroid Terrestrial-impact Last Alert System (ATLAS)

survey, and the Zwicky Transient Facility (ZTF), and the current number of TDEs has greatly increased to $\sim$100 (e.g., Gezari 2021; Hammerstein et al. 2023; Yao et al. 2023). Most of these TDEs are bright in optical/UV wavelengths but much fainter in X-rays, contrary to those earlier discovered TDEs. The origin of optical/UV emission is still under debate (e.g., Loeb & Ulmer 1997; Piran et al. 2015; Metzger & Stone 2016; Dai et al. 2018; Lu & Bonnerot 2020; Liu et al. 2021; Thomsen et al. 2022), awaiting the definitive observational evidence. As a result, the identification of optical/UV TDEs is empirical, relying on the features of the former samples.

A luckier star has a shallower encounter with an SMBH. Only part of it gets tidally disrupted and produces a similar flare. In this case, a partial TDE (pTDE) happens. The shallowness of the encounter is usually defined by the ratio of the tidal radius and the pericenter or the penetration factor, $\beta \equiv R_t/R_p$. Numerical simulations have found that the critical β values for the onset of the pTDE and the full TDE depend on the density profile of the star (e.g., Guillochon & Ramirez-Ruiz 2013; Law-Smith et al. 2017; Ryu et al. 2020a). The event rate for pTDEs is predicted to be comparable to or even higher than that of full TDEs (e.g., Stone & Metzger 2016; Ryu et al. 2020b; Stone et al. 2020; Chen & Shen 2021; Zhong et al.
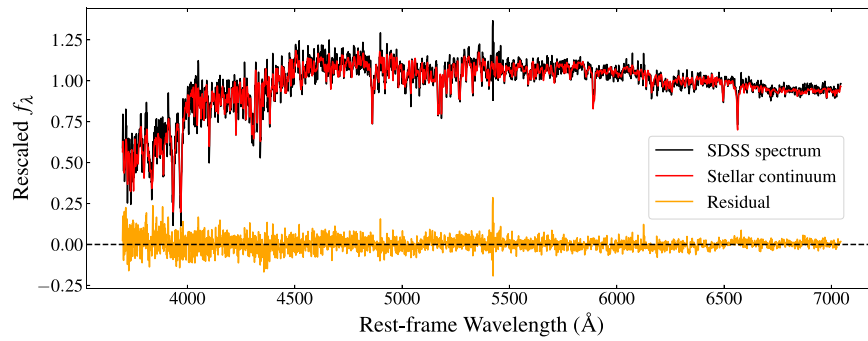
Figure 1. The pPXF fitting result of the SDSS host-galaxy spectrum. The residual shows no clear emission line, implying that the host galaxy should not be an AGN.

2022), providing a boost to the total TDE rate. However, distinguishing pTDEs from full TDEs is difficult, as the luminosity is not only determined by β or the disrupted mass but also depends on other parameters such as the radiation efficiency, black hole (BH) mass, and stellar properties.

Sometimes, this stroke of luck instead leads to tragedy. The unluckiest star initially has an elliptical orbit. Each time it approaches the pericenter, it experiences partial disruption, producing a series of flares. In this special case, a repeated pTDE occurs. The elliptical orbit of the star is possibly created by the Hills mechanism, in which a stellar binary passes by an SMBH and gets broken into a hypervelocity star and a tightly bound star (Hills 1988; Cufari et al. 2022; Lu & Quataert 2023). Repeated pTDEs can provide precious evidence for the existence of pTDEs. However, the confirmation of repeated pTDEs can be complicated by other possible scenarios, such as a double TDE caused by an extremely close encounter between a stellar binary and either an SMBH (Mandel & Levin 2015) or a milliparsec-scale SMBH binary (Wu & Yuan 2018). Alternatively, multiple independent TDEs could be supported by an enhanced TDE rate due to the concentrated nuclear stellar profile, e.g., in post-starburst galaxies (e.g., Arcavi et al. 2014; Hammerstein et al. 2021; Bortolas 2022; Wang et al. 2024) or galaxies with nuclear star clusters (Pfister et al. 2020). Despite the challenges, several candidates for repeated pTDE have been reported, e.g., IC 3599 (Campana et al. 2015), ASASSN-14ko (Payne et al. 2021, 2022, 2023; Huang et al. 2023), Swift J023017.0+283603 (Evans et al. 2023; Guolo et al. 2024b), eRASSt J045650.3–203750 (Z. Liu et al. 2023, 2024), AT 2018fyk (Wevers et al. 2023; Pasham et al. 2024), RX J133157.6–324319.7 (Hampel et al. 2022; Malyali et al. 2023), and AT 2020vdq (Somalwar et al. 2023b). The great diversity of the flaring intervals, bands, and shapes (listed in Table 2) among these sources calls for additional theoretical efforts.

In this Letter, we report the discovery of a new recurring flare at the position of AT 2022dbl (also known as AT 2018mac, ZTF18aabdajx, and ASASSN-22ci). It follows the dissipation of the tidal disruption flare that rose 2 yr ago. Photometric and spectroscopic follow-up observations have been conducted since this discovery, confirming that this flare is also the result of a TDE. Its extreme ~4100 Å emission line resembles the last flare, providing vital evidence for a repeated pTDE.

Since the discovery of the recurring flare on 2024 January 22, we have performed extensive photometric and spectroscopic observations. Meanwhile, we have also collected historical photometric and spectroscopic data to provide a comprehensive view of this event.

The Letter is organized as follows. In Appendix A, we present the observations and data reduction procedures. In Section 2, we analyze the host galaxy and the historical and recent photometric evolution in the UV, optical, and X-ray bands, as well as the optical spectra. In Section 3, we discuss the possible origins of AT 2022dbl and compare it with other repeated pTDEs. A final summary is given in Section 4. All errors marked with "±" represent the 1σ confidence intervals. We assume a flat cosmology with $H_0 = 70 \, \mathrm{km \, s^{-1} \, Mpc^{-1}}$ and $\Omega_\Lambda = 0.7$. For the extinction correction, we use the extinction law of Fitzpatrick (1999), the standard extinction curve with $R_V = A_V/E(B-V) = 3.1$ (Osterbrock & Ferland 2006), and adopt a Galactic extinction of $E(B-V) = 0.0159$ mag (Planck Collaboration et al. 2016). All magnitudes are in the AB system (Oke 1974).

2. Data Analysis

2.1. Host Galaxy

The host galaxy SDSS J122045.04+493304.6 has an early Sloan Digital Sky Survey (SDSS) spectrum. The redshift is $z = 0.02840 \pm 0.00001$. To examine the possible active galactic nucleus (AGN) activity, we fit the SDSS spectrum by the penalized pixel-fitting (pPXF) software (Cappellari 2023). We adopt the flexible stellar population synthesis model templates (Conroy et al. 2009) and mask the common galaxy emission and absorption lines before fitting the stellar continuum. The residual is obtained after subtracting the best-fit stellar continuum. As shown in Figure 1, the residual shows no clear emission line, which means that the host-galaxy spectrum can be fitted by a single stellar component. Therefore, the host galaxy should not be an AGN.

The velocity dispersion derived from the stellar continuum is $\sigma = 66.92 \pm 2.71 \, \mathrm{km \, s^{-1}}$. Using the relation of Kormendy & Ho (2013), we derive a BH mass of $\log(M_{\mathrm{BH}}/M_\odot) = 6.40 \pm 0.33$.

The spectrum displays Balmer absorption line series of Hα, Hβ, Hγ, and Hδ. We derive a Hα equivalent width (EW) emission of 0.015 ± 0.020 Å and a Lick Hδ_A index of 2.09 ± 0.44 Å. These parameters agree with the criteria of the quiescent Balmer-strong (QBS) galaxy: Hα EW emission <3 Å and H$\delta_A > 1.31$ Å (French et al. 2016).

2.2. UV/Optical Photometric Analysis

2.2.1. Historical Variability

To check if there was any variability before the 2022 outburst, we first query the differential photometric data of ZTF
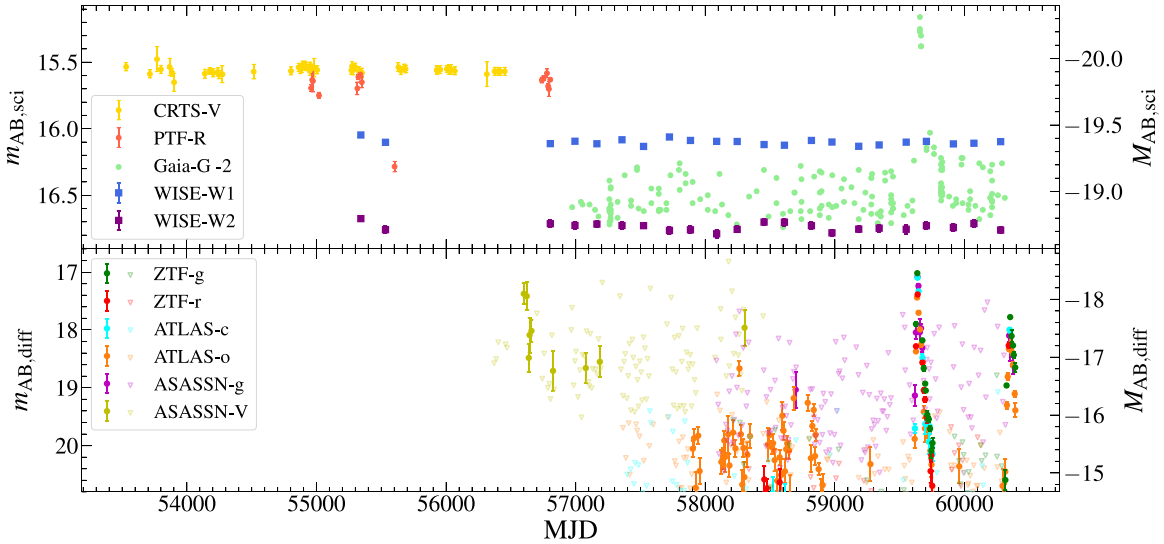
Figure 2. The historical light curves of the position of AT 2022dbl. Top panel: the non-host-subtracted light curves of three optical surveys, CRTS (V band), PTF (R band), and Gaia (G band), along with the MIR WISE survey (W1 and W2 bands). Bottom panel: the host-subtracted light curves of three optical surveys: ZTF (g and r bands), ATLAS (c and o bands), and ASAS-SN (g and V bands). To improve the SNR, we binned the data into 10 day bins for all optical bands except for Gaia G and approximately half-year bins for the W1 and W2 bands. Note that a potential early flare is displayed in the ASAS-SN V-band light curve; we discuss its reliability in Section 2.2.1.

(g and r bands), ATLAS (c and o bands), and ASAS-SN (g and V bands), as mentioned in Appendices A.1 and A.2. In addition, we query the Gaia Photometric Science Alerts (G band) and archival Catalina Real-Time Transient Survey (CRTS; V band) and Palomar Transient Facility (PTF; R band) catalogs, as introduced in Appendix A.4. In addition, we query the AllWISE and NEOWISE catalogs (mid-infrared, MIR, bands W1 and W2) and reduce the data using the method described in Appendix A.7. The reduced light curves are displayed in Figure 2. Before this outburst, there is no significant variability except for a potential flare, which is only shown in the ASAS-SN light curve at MJD $\sim$ 56600 (in 2013), $\sim$970 rest-frame days before the first peak. Although the peak magnitude is comparable to the 2022 outburst, it is just above the detection limit of ASAS-SN, and it is not included in the ASAS-SN transient list.[11] More importantly, no contemporary photometric or spectroscopic data can determine whether it is related to the recent nuclear outbursts or caused by a nearby supernova outburst, considering the large FWHM of $\sim$16″ for ASAS-SN (Jayasinghe et al. 2018, see also the ASAS-SN official website[12]). Therefore, we will not discuss this potential flare in the following text. For convenience, we refer to the flare that rose in 2022 as the "first flare" and the flare that rises in 2024 as the "second flare."

2.2.2. Light-curve Fitting

The optical/UV light curves during the first flare are displayed in the top panel of Figure 3. The rise stage of the first flare is well covered by the ATLAS o band. Since the peak, the light curves are well covered by the Swift Ultra-Violet/Optical Telescope (UVOT) observations, and the first epoch happens to be around the peak. Therefore, we set the peak time to the first Swift epoch $t_{\rm peak1} = $ (MJD) 59637.6. For the UV/optical light curves since the peak, we use the `Superbol` package (Nicholl 2018) to interpolate the light curves and fit all

photometry at each Swift epoch into a blackbody spectral energy distribution (SED). The best-fit results are displayed in Figure 4. The blackbody temperature $T_{\rm bb}$ slowly declines from $\sim$3 × 10^4 K to $\sim$2 × 10^4 K. The blackbody radius $R_{\rm bb}$ smoothly declines from $\sim$4 × 10^{14} cm to $\sim$1 × 10^{14} cm.

The optical/UV light curves during the second flare are displayed in the top panel of Figure 3. Its rise stage is well covered by the ZTF and Las Cumbres Observatory (LCO) g band. We choose the peak time as the brightest Swift epoch, $t_{\rm peak2} = $ (MJD) 60346.6, and perform the blackbody fitting on all photometry at Swift epochs except for the last one, which is apparently problematic. As shown in Figure 4, from -15 to $+30$ days, the blackbody temperature remains fairly constant at $\sim$26,000 K, while the blackbody luminosity evolves slowly, peaking $\sim$0.4 dex lower than the previous flare. Although the flat peak has been well covered by Swift, it has unfortunately entered safe mode since 2024 March 15, which was exactly when the source left the peak. After that, the decline stage is sparsely covered by the ZTF g and ATLAS o bands.

We characterize the light curves of both flares by the rest-frame rise time from half-peak luminosity to peak luminosity ($t_{1/2,\rm rise}$) and the decline time from peak luminosity to half-peak luminosity ($t_{1/2,\rm decline}$). To extract these two timescales, we fit the light curves with a Gaussian rise and a power-law decline:

$$L(t) = L(t_{\rm peak}) \times \begin{cases} e^{-(t-t_{\rm peak})^2/(2\sigma^2)}, & t < t_{\rm peak}; \\ \left(\dfrac{t - t_{\rm peak} + \tau}{\tau}\right)^{\alpha}, & t \geqslant t_{\rm peak}. \end{cases} \quad (1)$$

For the first flare, the rise and decline fittings are performed on the o-band and blackbody luminosity, respectively. For the second flare, the fitting is performed on the g-band luminosity. The best-fit light curves are drawn in the top panel of Figure 4, and the fitted parameters are listed in Table 1.

2.3. Optical Spectral Analysis

As introduced in Appendix A.6, three LCO spectra taken during the first flare were selected, while four optical spectra
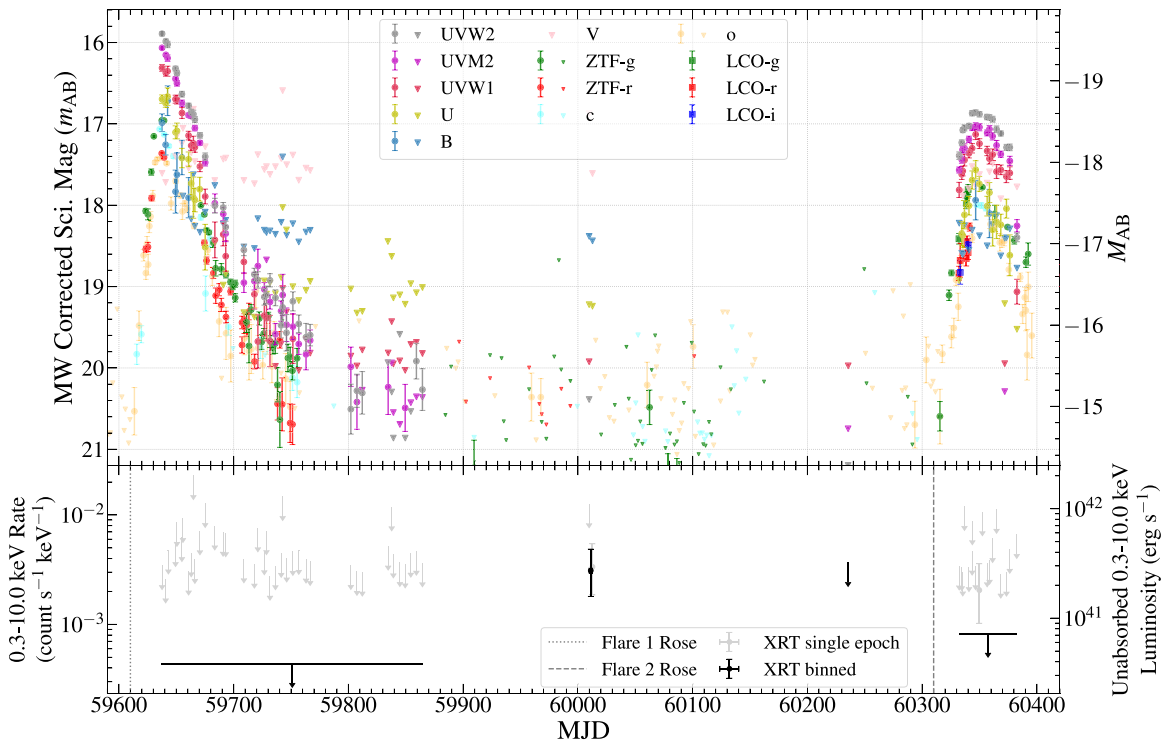

Figure 3. Top panel: the UV/optical light curves of AT 2022dbl during the first and second flares. 3σ upper limits are plotted in downward triangles. Bottom panel: the X-ray count rate of AT 2022dbl. The vertical dotted and dashed lines mark the approximate rise time of the first and second flares, respectively. 3σ upper limits are plotted in downward arrows.

have been taken during the second flare. In addition, an SDSS host spectrum is available. All of these spectra are shown in Figure 5. The spectral fitting procedures for each transient spectrum are listed as follows.

(1) Host-galaxy subtraction. Since the host spectrum displays clear Ca II absorption doublets at 3910–4000 Å, and the blue side has higher signal-to-noise ratio (SNR) than the red side, we used these doublets for calibration. We fit and subtract the nearby pseudocontinuum for both the transient and host spectra. Then a least-squares fitting on the residuals gives the multiplication factor for the host-galaxy component. Limited by the wavelength range of the host spectrum, we perform the fitting only within this range. The three representative LCO spectra were taken at MJD 59638 (+0 day), MJD 59664 (+26 days), and MJD 59690 (+51 days). The two spectra taken by the Himalayan Chandra Telescope (HCT) at the early stage of the second flare are discarded, as their SNRs are too low for the host-galaxy subtraction and also for further analysis.

(2) Continuum fitting. After subtracting the host component, a power-law function is used to fit the continuum. In the case of LCO spectra, the continuum windows are set to the following line-free regions (in rest-frame wavelengths): 3700–3900 Å, 5200–5400 Å, 6100–6300 Å, 7100–7400 Å, and 7600–8490 Å, with the exclusion of the telluric absorption regions. For the spectra taken by the 200-inch Hale telescope at the Palomar Observatory (P200), the continuum and telluric absorption regions are a bit different (see Figure B1).

(3) Line fitting. After subtracting the continuum, all residuals exhibit multiple broad characteristics around 3900–4200 Å,

4400–5200 Å, and 6300–6900 Å, some showing a faint broad bump around 5500–6100 Å. The broad feature in the 3900–4200 Å range is symmetrical and peaks at approximately 4100 Å, possibly corresponding to N III (4100) or Hδ (4101). In the range 4400–5200 Å, the characteristic is asymmetric and could be a combination of N III (4640), He II (4686), and Hβ (4861). Lastly, the broad feature in the range 6300–6900 Å is symmetric and centers around 6560 Å. It is consistent with a broad Hα (6563) emission line. The 5500–6100 Å feature can be tentatively interpreted as He I (5876). The selection of the fitting components is based on these facts. First, the extended red wing of the 4400–5200 Å feature indicates the existence of Hβ, which is further supported by the existence of Hα. Second, it is unlikely that the 3900–4200 Å bump is dominated by Hδ, since Hα is too weak compared to this feature. Therefore, it should be dominated by N III (4100), although the Hδ will slightly affect the intensity. The N III $\lambda4100$ lines are usually produced by the Bowen mechanism, which requires He II Lyα lines at 304 Å. Taking into account the extreme strength of N III $\lambda4100$, the He II emission should be strong. Moreover, the N III $\lambda4640$ lines should also be produced via this mechanism. Therefore, both the He II $\lambda4686$ line and the N III $\lambda4640$ line should be considered. In addition, a He I $\lambda5876$ component is involved to cover the weak emission features in several spectra. To ensure reliability, the FWHM and the offset of the two features of N III are tied up, as do those of Hα and Hβ. The fitting results are shown in Figure B1.

Despite careful selection of fitting components, the 4400–5200 Å feature is still hard to deblend due to its smoothness; hence, it
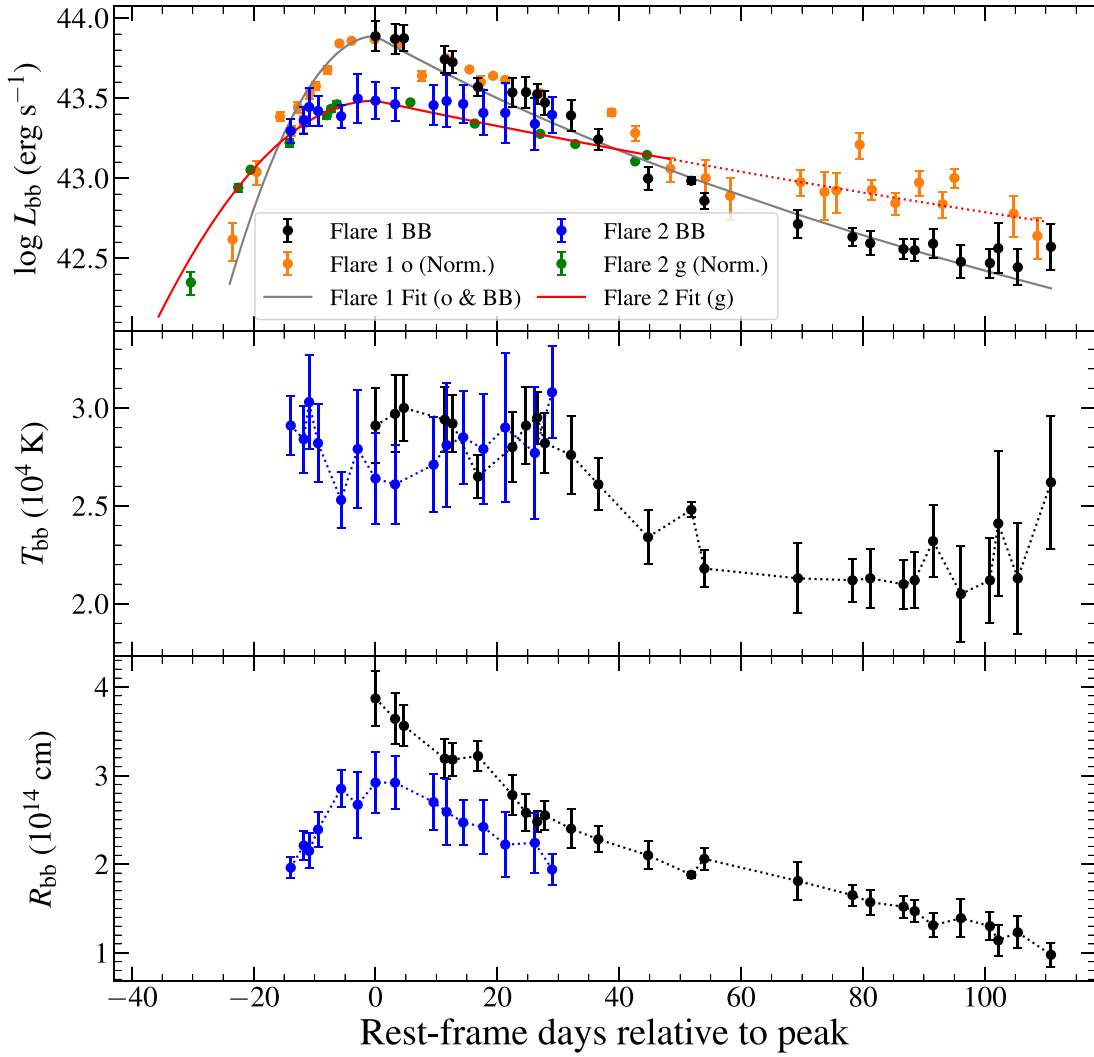
Figure 4. The light-curve fitting results of AT 2022dbl. The luminosities of the o and g bands are normalized to the blackbody luminosities of the first and second flares, respectively. For comparison, the fitted decline curve for the second flare is extended to $\sim +120$ days in the dotted style.

Table 1
The Best-fit Light-curve Parameters for the Two Flares

| Flare (No.)	$t_{\rm peak}$ (MJD)	$L_{\rm BB,peak}$ (log (erg s^{-1}))	$T_{\rm BB,peak}$ (10^4 K)	$R_{\rm BB,peak}$ (10^{14} cm)	$t_{1/2,\rm rise}$ (days)	$t_{1/2,\rm decline}$ (days)
1	59637.6	43.89 ± 0.10	2.91 ± 0.19	3.87 ± 0.31	10.6 ± 0.5	15.7 ± 0.8
2	60346.6	43.48 ± 0.12	2.64 ± 0.23	2.92 ± 0.34	16.8 ± 0.5	36.9 ± 2.4

Note. $t_{1/2,\rm rise}$: the rest-frame rise time from half-peak luminosity to peak luminosity. $t_{1/2,\rm decline}$: the rest-frame decline time from peak luminosity to half-peak luminosity.

cannot prove or disprove the existence of He II $\lambda 4686$ and the associated Bowen mechanism as well as the intensity of N III $\lambda 4640$. Therefore, we only focus on the evolution of the most prominent and unblended features: N III $\lambda 4100$ and Hα. Furthermore, we also examine the power-law indexes of the continua. Figure 6 illustrates the evolution of the FWHM, velocity shift, and luminosity of N III $\lambda 4100$ and Hα emission lines, along with the power-law indexes of the continua, during both flares.

For the LCO spectra taken during the first flare, the FWHMs for the Hα lines in all spectra are well above 10,000 km s^{-1}, showing a slowly narrowing trend from FWHM $\sim 18,000$ to $\sim 12,000$ km s^{-1} during $+0$ day to $+51$ days to the first peak. N III $\lambda 4100$ shows a narrowing trend from FWHM $\sim 12,000$ to

~ 9000 km s^{-1}. Except for the first epoch, neither of the N III $\lambda 4100$ lines nor Hα exhibit clear shifts toward blue or red. The luminosity of Hα and N III $\lambda 4100$ gets lower at later phases. The high N III $\lambda 4100$ luminosity of $\sim 10^{41}$ erg s^{-1} and the evolution of the N III $\lambda 4100$/Hα ratio highly resemble AT 2018dyb, which has the highest N III $\lambda 4100$ luminosity among spectroscopically confirmed TDEs (Leloudas et al. 2019; Charalampopoulos et al. 2022). We note that the precision of the luminosity depends on the flux calibration. The continuum gets flatter as it gets fainter.

For the first P200 spectrum (-6 days to the second peak), it displays an Hα emission line with FWHM $\sim 10,000$ km s^{-1} and N III $\lambda 4100$ with FWHM $\sim 13,000$ km s^{-1}, while the
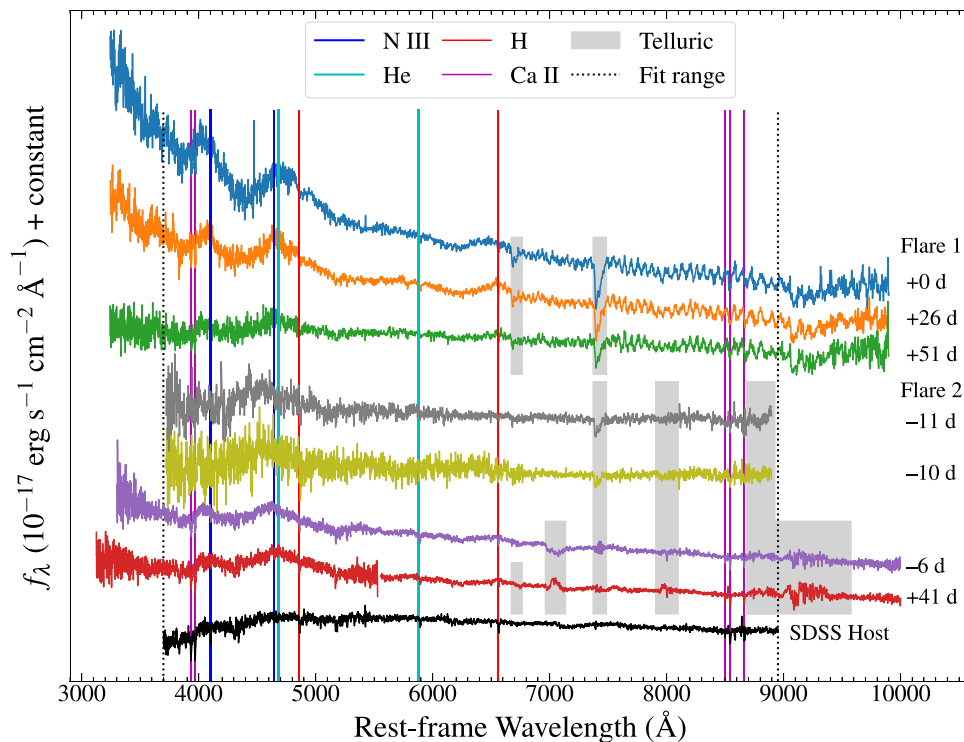
Figure 5. The optical spectra of AT 2022dbl. Black dotted lines limit the range of the spectral fitting.
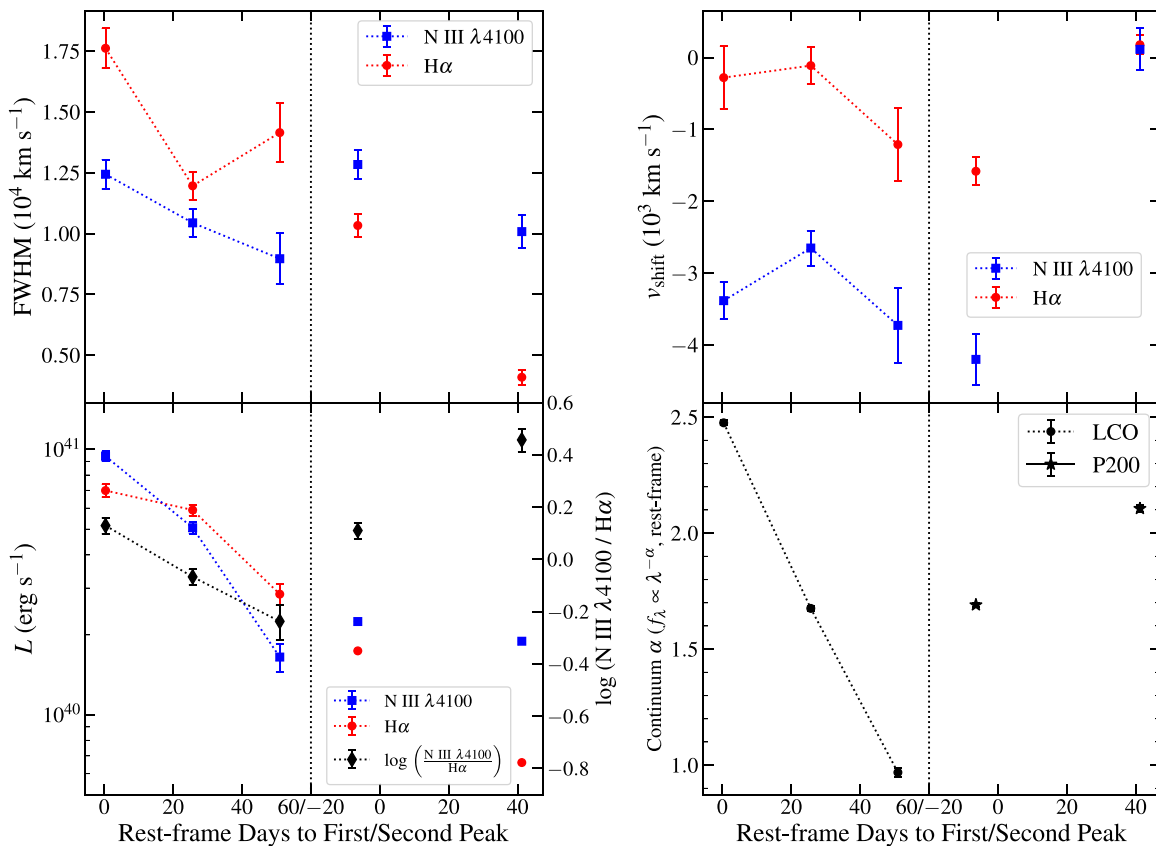
Figure 6. The evolution of the FWHM, velocity shift, and luminosity of the N III $\lambda4100$ (blue squares) and Hα (red dots) emission lines as well as their ratios (black diamonds) and the power-law indexes of the continua. In the last panel, measurements from the LCO spectra taken during the first flare and P200 spectra taken during the second flare are marked in dots and asterisks, respectively.

velocity shift and luminosity for both lines are similar to the late-time spectra of the previous flare. The power-law index for the continuum rises again, which is consistent with a newly risen flare. The second P200 spectrum displays a much narrower and weaker Hα feature with FWHM ~ 4000 km s^{-1} and a luminosity of $<10^{40}$ erg s^{-1}, which fades much quicker than the N III $\lambda 4100$ feature. As a result, the ratio N III $\lambda 4100$/Hα increases to $\gtrsim 1$. The power-law index for the continuum is higher than that of the previous spectrum.

2.4. X-Ray Luminosity Estimation

As described in Appendix A.5, X-ray observations were made with the Swift X-Ray Telescope (XRT) during both flares. All X-ray epochs are divided into four segments, as shown in the bottom panel of Figure 3. Only one segment yields a marginal detection with a rate-to-error ratio of ~ 2, which does not allow for spectral analysis (bottom panel of Figure 3). The stacked image of the first phase (0 day to +220 days relative to the first peak) yields a total exposure time of 78.7 ks and a tight 3σ upper limit for the 0.3–10.0 keV count rate of 4.37×10^{-4} counts s^{-1}. Assuming a typical blackbody model of $kT = 50$ eV (e.g., Guolo et al. 2024a) and a hydrogen column density of $N_H = 1.94 \times 10^{20}$ cm^{-2} (HI4PI Collaboration et al. 2016), we obtain an upper limit for the unabsorbed luminosity using the WebPIMMS tool[13] of $L_{X,1} < 3.8 \times 10^{40}$ erg s^{-1}. Following the same method, we derive the luminosity for the later three segments: $L_{X,2} = 2.7^{+1.5}_{-1.1} \times 10^{41}$ erg s^{-1}, $L_{X,3} < 3.2 \times 10^{41}$ erg s^{-1}, and $L_{X,4} < 7.2 \times 10^{40}$ erg s^{-1}.

3. Discussion

3.1. AT 2022dbl as a Robust Repeated pTDE

We shall discuss the origin of these two flares as follows. As displayed in Section 2.1, the preoutburst SDSS spectrum exhibits a series of strong Balmer absorption lines and shows no clear emission line after subtracting the best-fit stellar continuum. Combined with the lack of strong historical radio, X-ray, and MIR variability, as well as the MIR $W1 - W2$ color of 0.007 that against the AGN criterion, the presence of a persistent AGN can be firmly excluded. In addition, the first flare lasted less than 1 yr, which is unusual for a turn-on AGN, and the second flare showed a number of similar photometric and spectroscopic features. We thereby reject the possibility of an AGN origin for both flares. On the other hand, both flares show broad Hα emission with FWHM $> 10,000$ km s^{-1} and declining blackbody radii after the peak, which also strongly contradicts the SN origin.

All of the features that disfavor AGNs and supernovae are nevertheless characteristic of TDEs, including the timescales of both flares, the fairly steady blackbody temperatures of $(2–3) \times 10^4$ K, the value and evolution of the blackbody radii, and the very broad Hα emission. Therefore, AT 2022dbl is undoubtedly a repeated TDE. Moreover, both flares display highly similar broad Hα, $\sim 4400-5200$ Å (Hβ and possible N III and He II), and ~ 4100 Å (N III and possible Hδ) features, as shown in Figure 7. In particular, for both flares, the luminosity of ~ 4100 Å is comparable to that of Hα (see the lower left panel of Figure 6), which is rare among all TDEs. Hence, these two flares probably originated from the debris of a single disrupted star, and AT 2022dbl should be a robust repeated pTDE.

We now try to rebuild the orbit of this "unluckiest star" before it got stripped by the BH. Assuming a BH mass of $10^{6.40} M_\odot$ and an elliptical orbit with a period of ~ 710 days, the semimajor axis of the orbit should be log a (cm) = 15.5, or $a \approx 210$ au. For a solar-like star, the tidal radius should be log R_t (cm) = 13.0, or $R_t \approx 0.6$ au. Hence, the eccentricity is $e = 1 - R_p/a \sim 1 - R_t/a \approx 0.997$. Based on this result, we tentatively propose a scenario for repeated pTDEs at the end of Section 3.3.

3.2. Comparison with Other Repeated pTDEs and Common Optical TDEs

As mentioned in Section 1, several repeated pTDE candidates have been reported in the literature: IC 3599, ASASSN-14ko, eRASSt J045650.3–203750, Swift J023017.0 +283603, AT 2018fyk, RX J133157.6–324319.7, and AT 2020vdq. We briefly list the information of these repeated pTDEs in Table 2.

As shown in the table, only ASASSN-14ko, AT 2020vdq, and AT 2022dbl show recurring flares in optical bands. We only focus on the comparison of AT 2020vdq and AT 2022dbl, as they share similar intervals and host-galaxy types, while the behavior of ASASSN-14ko differs greatly. We compare the peak blackbody luminosity and radius and the rise and decline timescales of AT 2022dbl with those of AT 2020vdq and other ZTF TDEs listed in Yao et al. (2023), as plotted in Figure 8.

AT 2022dbl shows several differences compared to AT 2020vdq. First, its peak luminosity for the second flare is ~ 0.4 dex lower than that of the first flare, while for AT 2020vdq, the peak luminosity of the second flare is ~ 1.2 dex higher than that of the first flare. Second, for AT 2022dbl, the second flare rises and declines slower than the first flare. In contrast, for AT 2020vdq, the second flare rises and declines much more quickly than the first flare.

We compare AT 2020vdq and AT 2022dbl with the ZTF TDEs (Yao et al. 2023) that show no recurrent flare by now. For AT 2020vdq, the peak luminosities of its first flare are the lowest and the second-lowest among all optical TDEs, while the rise and decline timescales of its second flare are the lowest and the second-lowest among all optical TDEs. In short, both flares of AT 2020vdq show some peculiarities compared to normal TDEs. For AT 2022dbl, its peak blackbody radius is the smallest among all TDEs with $6 \leqslant$ log $(M_{BH}/M_\odot) \leqslant 7$. Apart from this, its peak luminosity and rise and decline timescales of both flares are all typical among the ZTF TDEs. Therefore, the two flares of AT 2022dbl are both typical tidal disruption flares.

3.3. Robustness of a "Repeated pTDE" Classification

As introduced in Section 1, the identification of a repeated pTDE can be complicated by some alternative origins. Hence, a robust identification of a repeated pTDE (especially an optical one) is difficult. It requires not only confirmation of the TDE origin but also a trustworthy connection between the flares.

As an example, we examine the case of AT 2020vdq. In Somalwar et al. (2023a), the authors establish the TDE origin for the first flare by the broadband light curve, the newly risen radio flare, the E+A host galaxy, and the intermediate-width ($\sim 700-1000$ km s^{-1}) Balmer, He II, He I, and [Fe X] emission in the late-time spectra ($\sim +600$ days). In Somalwar et al.

---

[13] https://heasarc.gsfc.nasa.gov/cgi-bin/Tools/w3pimms/w3pimms.pl
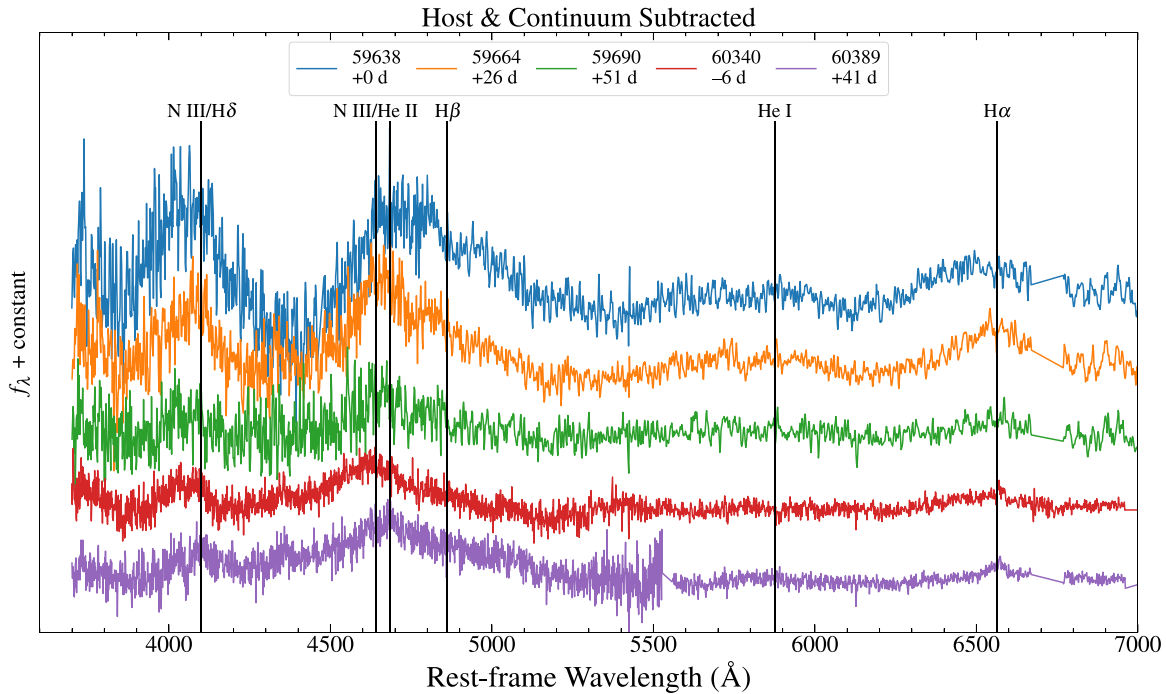
Figure 7. Spectra after subtracting the host-galaxy contribution and the continuum. Spectra of both flares show similar emission lines.

Table 2
List of Published Repeated pTDE Candidates

Name	Host Type	Band	Period/Interval (Days)	Flares	Peak Evolution
ASASSN-14ko (1, 2, 3, 4)	Seyfert 2	Opt./UV/X-ray[†]	115.2	∼30	Similar
Swift J023017.0+283603 (5, 6)	Weak AGN	X-ray	∼22	∼11	Variable
eRASSt J045650.3–203750 (7, 8)	Quiescent	X-ray/UV[†]	299 → 193	5	Lower
IC 3599 (9, 10, 11, 12, 13)	Seyfert 1.9	X-ray/opt.[*]	∼3470[?]	2/3	Similar
AT 2018fyk (14, 15, 16)	Quiescent	UV/X-ray	∼1200	2	Lower
RX J133157.6–324319.7 (17, 18)	Quiescent	X-ray	∼10,000	2	Similar
AT 2020vdq (19, 20, 21)	E+A	Opt./UV[*]/X-ray[*]	∼870	2	Higher
AT 2022dbl (22)	QBS	Opt./UV	∼710	2	Lower

Note. Band: [†] not periodic; [*] not observed during the first flare. Period/interval: ASASSN-14ko shows a nearly constant period of 115.2 days. Swift J023017.0 +283603 shows a period of ∼22 days. eRASSt J045650.3–203750 has shown five flares with the interval declining from 299 to ∼193 days. Other sources show only two flares. [?] IC 3599 showed two prominent X-ray flares in 1990 and 2010. Campana et al. (2015) predicted a 9.5 yr period in a repeated pTDE scenario, suggesting a missing flare between the two flares. However, Grupe et al. (2024) reported that another X-ray flare did not come in the predicted time window. Peak evolution: the peak luminosity of the earlier flare vs. that of the later flare.
References. (1) Payne et al. (2021), (2) Payne et al. (2022), (3) Payne et al. (2023), (4) Huang et al. (2023), (5) Evans et al. (2023), (6) Guolo et al. (2024b), (7) Liu et al. (2023), (8) Z. Liu et al. (2024), (9) Grupe et al. (1995), (10) Komossa & Bade (1999), (11) Grupe et al. (2015), (12) Campana et al. (2015), (13) Grupe et al. (2024), (14) Wevers et al. (2019), (15) Wevers et al. (2023), (16) Pasham et al. (2024), (17) Hampel et al. (2022), (18) Malyali et al. (2023), (19) Yao et al. (2023), (20) Somalwar et al. (2023a), (21) Somalwar et al. (2023b), (22) this work.

(2023b), the second flare is spectroscopically identified as a TDE, since the spectra around the peak exhibit broad (∼20,000 km s⁻¹) Balmer, He II, and He I emission lines. Although the TDE H+He identification for both flares is reliable, the two flares show highly different peak luminosities and light-curve shapes and have no contemporary spectra to support their physical connection. Moreover, the E+A host galaxy may have a much higher TDE rate than normal galaxies (Arcavi et al. 2014; French et al. 2016; Hammerstein et al. 2021). In an extreme case, the probability of detecting two independent TDEs within ∼3 yr can be as high as 30% (see Section 5.1 of Somalwar et al. 2023b).

In the case of AT 2022dbl, its two flares not only exhibit photometric and spectroscopic features that firmly establish their TDE origins but also display similar broad Balmer, N III, and possible He II emission lines in the early spectra of both flares, strongly indicating a connection between them (see Figure 7). This represents the first robust spectroscopic evidence for a repeated pTDE.

This spectroscopic evidence is important for the repeated pTDE classification, as current photometric data for both events cannot provide enough support. On the one hand, there are only two flares in both events, allowing for alternative origins, especially independent TDEs, as their host galaxies can have higher TDE rates than normal galaxies. On the other hand, the light curves can provide limited information on the judgment of repeated pTDEs by now, as there is currently a lack of reliable optical/UV repeated pTDEs for comparison. A third flare can

(a)

(b)

(c)
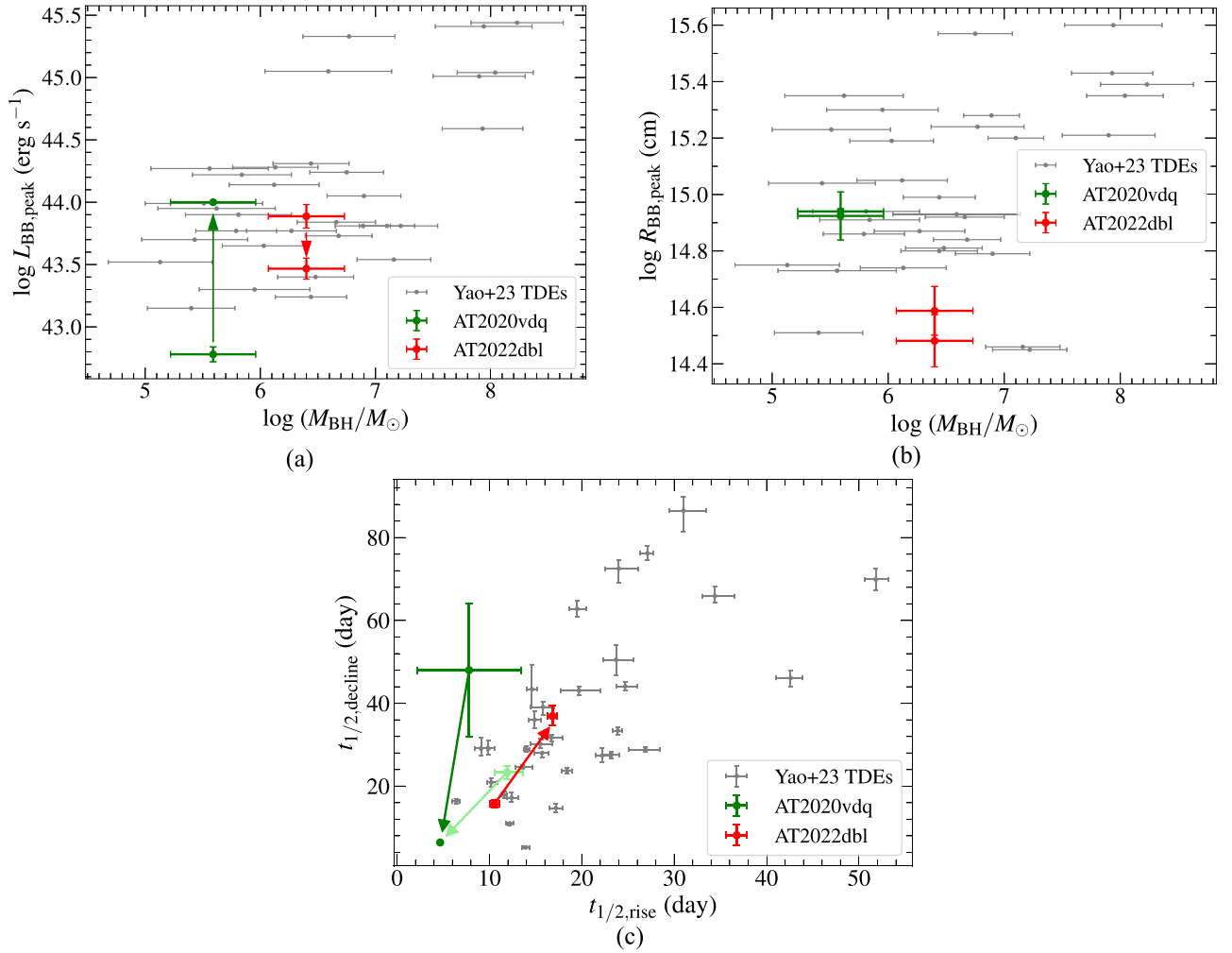
Figure 8. Comparison of optical repeated pTDEs AT 2020vdq (Somalwar et al. 2023b; Yao et al. 2023) and AT 2022dbl (this work), as well as optical TDEs listed in Yao et al. (2023). BH mass vs. (a) peak blackbody luminosity, (b) peak blackbody radius, and (c) rest-frame rise time from half-peak luminosity to peak luminosity vs. decline time from peak luminosity to half-peak luminosity. In plot (b), both AT 2020vdq and AT 2022dbl show similar blackbody radii in their two flares. The parameters of AT 2020vdq are mostly adopted or derived from Somalwar et al. (2023b). However, in plot (c), the derived rise and decline timescales of the first flare of AT 2020vdq in Somalwar et al. (2023b) and Yao et al. (2023) are greatly different and hence plotted in green and light green, respectively.

provide conclusive evidence for a repeated pTDE classification, which might occur in the next couple of years.

We notice that recent simulation works of repeated pTDEs (e.g., Bandopadhyay et al. 2024; C. Liu et al. 2024) have reproduced the light-curve patterns similar as ASASSN-14ko, AT 2020vdq, and AT 2022dbl under several sets of stellar parameters (e.g., mass and age) and β. These results are heuristic but still preliminary, as the parameter space remains to be fully explored. If the simulation sets can be extended to a grid, we can constrain the stellar parameters and β and predict the future evolution.

As illustrated in Figure 8(b), for both events, their two flares share a similar peak blackbody radius. The radius for AT 2022dbl is $\log R_{bb}$ (cm) ~ 14.5, which lies between the tidal radius, $\log R_t$ (cm) $= 13.0$, and the semimajor axis, $\log a$ (cm) $= 15.5$. This relation is also found in AT 2020vdq: $\log R_{bb}$ (cm) ~ 14.9, $\log R_t$ (cm) $= 12.7$, $\log a$ (cm) $= 15.3$. This similarity provides additional support for a pTDE claim, as it suggests the connection between these two flares. Based on the relation, we tentatively propose this scenario. The star shallowly encounters the SMBH and loses a small fraction of mass, then leaves the tidal radius with the orbit largely

unaffected. As a result, the bound debris can self-intersect at a similar radius, which is far away from both the pericenter and apocenter. Additional theoretical works and numerical simulations are encouraged to test this scenario.

4. Conclusion

We have reported the discovery of a repeated pTDE, AT 2022dbl, in a nearby quiescent galaxy. In this event, two separate flares occurred in 2022 and 2024, with an interval of ~ 710 days. Both flares have been fortunately followed by high-cadence optical/UV photometry and X-ray observations, as well as a series of optical spectroscopy observations, which help to confirm the TDE origin for both flares. More importantly, similar broad Balmer, N III, and possible He II emission lines, especially the extreme ~ 4100 Å emission lines, help to rule out the possibility of two independent TDEs and provide the first robust spectroscopic evidence for two tidal disruptions of the same star.

Both flares of AT 2022dbl are bright in optical/UV wavelengths but much fainter in X-rays, which are similar to most TDEs that were found in optical surveys in the past decade. Repeated pTDEs, particularly optical/UV-bright TDEs

like AT 2022dbl, provide valuable opportunities to test optical/ UV emission models, as another flare is expected in the coming years. Its repeatability enables us to carefully plan for multiwavelength observations of subsequent flares from the earliest stages. With the assistance of high-cadence optical/ UV/X-ray photometric and spectroscopic data, we can take the chance to collect important clues to the mechanism of optical/ UV emission of TDEs, as well as the associated "missing energy" problem (Piran et al. 2015; Lu & Kumar 2018). As the next-generation "TDE hunters" come into play, such as the Vera Rubin Observatory (Ivezić et al. 2019) and the Wide Field Survey Telescope (Lin et al. 2022; Wang et al. 2023), the high-cadence multiband surveys are expected to reveal a number of such pTDEs and accelerate the process of solving these puzzles in the near future.

Appendix A
Observation and Data Reduction

A.1. ZTF Optical Photometry

The ZTF differential point-spread function (PSF) photometry of AT 2022dbl is obtained through the ZTF forced-photometry

Table A1
Host-galaxy Photometry Used in the SED Fitting

Catalog	Band	λ_{eff} (nm)	Flux (mJy)
GALEX	FUV	153	0.004 ± 0.001
GALEX	NUV	227	0.023 ± 0.001
SDSS	u	355	0.346 ± 0.006
SDSS	g	467	1.311 ± 0.004
SDSS	r	616	2.388 ± 0.007
SDSS	i	747	3.207 ± 0.009
SDSS	z	892	3.994 ± 0.023
2MASS	J	1232	3.947 ± 0.386
2MASS	H	1642	4.554 ± 0.566
2MASS	K_s	2157	4.432 ± 0.624
WISE	W1	3346	1.394 ± 0.033
WISE	W2	4595	0.771 ± 0.021

service (Masci et al. 2019). We clean the photometry results by filtering out epochs that are impacted by bad pixels and requiring thresholds for the SNR of the observations, seeing, zero-point, the sigma per pixel in the input science image, and the 1σ uncertainty on the difference image photometry measurement. We perform the baseline correction by the following two steps. First, we classify the measurements by the field, charge-coupled device, and quadrant identifiers. Then, for each class, we set the median of the preoutburst counts as the offset. After that, we build the ZTF g- and r-band light curves for AT 2022dbl. AT 2022dbl was first alerted by ZTF in 2018 March, got the internal name ZTF18aabdajx, and was reported to the Transient Name Server as AT 2018mac. However, we carefully examine the light curves and confirm a false alert, which may be a temporary problem during the early test of ZTF.

A.2. ATLAS and ASAS-SN Optical Photometry

We obtain the ATLAS differential photometry from the ATLAS forced-photometry server (Tonry et al. 2018; Smith et al. 2020; Shingles et al. 2021). To improve the SNR, we combine the data into 1 day bins and build the ATLAS c- and o-band light curves. Meanwhile, we obtain ASAS-SN differential photometry from the ASAS-SN sky patrol (Shappee et al. 2014; Kochanek et al. 2017). The Galactic-extinction-corrected light curves are shown in the top panel of Figure 3.

A.3. LCO Optical Photometry

From 2024 January 22 to 2024 January 31, we conducted optical monitoring using the LCO Global Telescope network (Brown et al. 2013) in the u, g, r, and i bands with daily cadence. With the same method as Zhu et al. (2023), we use PanSTARRS (Flewelling et al. 2020) gri-band stack images as reference images and employ `HOTPANTS` (Becker 2015) for image subtraction. After image subtraction, we perform PSF photometry on the difference image, and the photometric results are calibrated using PS1 standards in the field of view. The Galactic extinction-corrected photometric measurements are plotted in the top panel of Figure 3.

A.4. Gaia, CRTS, and PTF Optical Photometry

To check historical variability, we query the Gaia Photometric Science Alerts and the CRTS (Drake et al. 2009) and PTF catalogs. To improve SNR, we combine the CRTS and

PTF data into 10 day bins. The results are displayed and discussed in Section 2.2.1.

A.5. Swift UVOT and XRT Observations

The previous flare was fortunately well covered by Swift observations. During the previous flare, observations were performed by the XRT (Burrows et al. 2005) and the UVOT (Roming et al. 2005) on Swift under a great number of target-of-opportunity (ToO) requests (ObsID: 00015026001-00015026045; PIs: Arcavi/Hinkle/Jiang/Makrygianni/Holoien/Margutti). The recent flare had been well followed under several ToO requests (ObsID: 00015026046-00015026064; PIs: Lin/Hammerstein) before Swift unfortunately entered the safe mode on 2024 March 15. We retrieve the Swift data from HEASARC[14] and process all data with `heasoft` v6.30.1. Details are described below.

For each UVOT epoch, we first examine each image file and exclude the extensions with bad photometric flags. For image files with multiple valid extensions, we sum all extensions using the task `uvotimsum`. Then, the task `uvotsource` performs photometry on each image, with the source and source-free background region defined by a circle of a radius of $20''$ and $40''$, respectively. The host contribution is estimated via SED fitting. We collect the photometry from the Galaxy Evolution Explorer (GALEX; Martin et al. 2005) General Release 6, the SDSS Data Release 16 (DR16; Ahumada et al. 2020), the Two Micron All-Sky Survey (2MASS; Skrutskie et al. 2006), and the AllWISE catalog (Cutri et al. 2021), listed in Table A1. After correcting the Galactic extinction, we fit the SED by running the dynamic nested sampler `dynesty` (Speagle 2020) under the `prospector` package (Johnson et al. 2021). The best-fit SED and synthetic UVOT magnitudes are plotted in Figure A1. The stellar mass derived from the posterior distribution is $\sim 10^{10.47}\,M_\odot$, corresponding to a BH mass of $\sim 10^{6.89 \pm 0.26}\,M_\odot$ via the Reines & Volonteri (2015) method.

For each XRT epoch, we reduce the data by `xrtpipeline` and obtain the level 2 products. Then we use `xrtproducts` to extract the level 3 products. After that, we use `xselect` to stack all images. On this stacked image, no discernible source is shown at the position of the transient. To obtain an upper limit, the source region is selected as a circle of radius $20''$, while the background region is defined as a source-free annulus with an inner radius of $50''$ and an outer radius of $150''$. We obtain the source and background photon counts in 0.3–10 keV by `ximage`. For images with photon counts in the source region $N \leqslant 80$, a Bayesian approach is applied to calculate the 3σ lower and upper limits (Kraft et al. 1991), while for $N > 80$, a Gaussian approach is adopted (Evans et al. 2007, 2009; König et al. 2022). Based on single-epoch photometric results, we divide all epochs into four segments. (1) Epochs before MJD 59900. All of the results are upper limits, so we stack all images to get a tighter upper limit. The total exposure time is 78.7 ks. (2) Epochs between MJD 60000 and 60030. The two epochs are isolated from the others; one of them yields a tentative detection with a rate-to-error ratio of ~ 2. The total exposure time is only 2.3 ks. (3) One epoch on MJD 60235. It is just before the rise of the second flare (MJD ~ 60310), with an exposure time of 4.15 ks. (4) Since MJD 60310. Only one epoch reveals a tentative detection with a rate-to-error ratio of ~ 2, and the total exposure time is 34.7 ks. The X-ray light
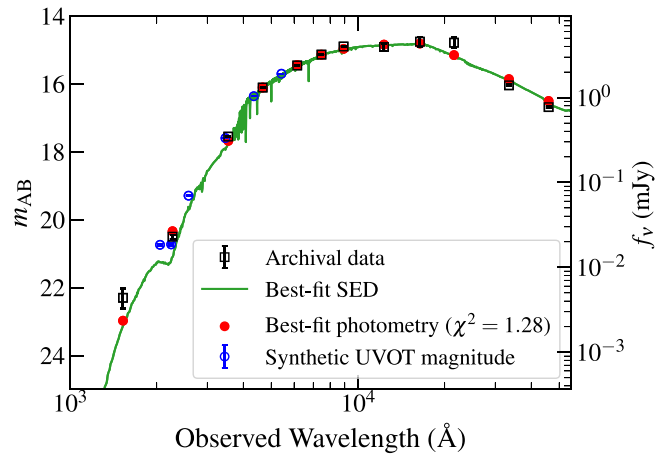
Figure A1. The SED fitting result of the `prospector` package, in units of AB magnitudes. The best-fit SED and photometry are plotted in green and red, respectively. The blue circles represent the synthetic magnitudes of the UVOT UVW2, UVM2, UVW1, U, B, and V bands.

curve is displayed in the bottom panel of Figure 3. The low SNR impedes us from further analysis; a brief luminosity estimation is introduced in Section 2.4.

A.6. Optical Spectroscopy

Since the discovery of the recurrent flare, we have obtained two spectra using the Double Spectrograph (DBSP; Oke & Gunn 1982) on P200 and two spectra using the Himalaya Faint Object Spectrograph instrument mounted on the 2 m HCT of the Indian Astronomical Observatory (Prabhu 2014). The spectroscopic data are reduced in a standard manner using the packages in `IRAF` with the aid of the Python scripts hosted at `REDPIPE` (Singh 2021). We use the `pypeit` package (Prochaska et al. 2020) to reduce the P200/DBSP spectra and extract the HCT spectra by `IRAF`. As we retrieve the LCO photometric data, we find 12 automatically reduced public spectra taken by the 2.0 m telescope at Haleakala Observatory during the previous flare (Proposals: CON2022A-007/HAW2022A-002).[15] We use three high-quality representative spectra of them, which are introduced and analyzed in Section 2.3.

A.7. WISE MIR Photometry

AT 2022dbl has been continuously observed by the Wide-field Infrared Survey Explorer (WISE; Wright et al. 2010) and the successive Near Earth Object Wide-field Infrared Survey Explorer (NEOWISE; Mainzer et al. 2011, 2014) at the W1 (3.4 μm) and W2 (4.6 μm) bands every half-year.

To check the potential MIR dust echo (Jiang et al. 2016; van Velzen et al. 2016), we query and download the W1- and W2-band photometric data from the AllWISE Multiepoch Photometry Table and the NEOWISE-R Single Exposure (L1b) Source Table. We filter out the bad data points that have NaN magnitudes and errors or get affected by a nearby image artifact (`cc_flags` $\neq 0$), scattered moonlight (`moon_masked` $\neq 0$), or a nearby detection (`nb > 1`). The remaining data points are grouped into approximately half-year bins to enhance the SNR. No variability has been detected in the four epochs since the

---

[14] https://heasarc.gsfc.nasa.gov/cgi-bin/W3Browse/swift.pl

[15] These spectra can be retrieved from the LCO Science Archive: https://archive.lco.global.

rise of the previous flare (MJD ∼ 59706−60279). The averaged W1−W2 Vega magnitude for the host galaxy is 0.007 ± 0.006. This results is consistent with Jiang et al. (2021), who found that most optical TDEs show very weak IR echoes likely due to a very low dust covering factor, while the W1−W2 color is against the AGN selection criterion: W1 − W2 ⩾ 0.8 (Stern et al. 2012).

A.8. Radio Observations

According to Sfaradi et al. (2022),[16] on 2022 February 26 (around the peak of the previous flare), a 2 hr Very Large Array (VLA) observation revealed a single faint point source with flux density of $32 \pm 7\,\mu$Jy in the Ku band ($\nu \sim 15$ GHz). The distance is $\sim 0.''4$ from the reported position of AT 2022dbl, which is consistent with the position of the center of the host galaxy. However, the data are not publicly available.

Furthermore, the position of AT 2022dbl has also been observed by the VLA Sky Survey (VLASS; Lacy et al. 2020) three times. Two of the observations were performed before the flare: epoch 1.1 on 2017 November 20 and epoch 2.1 on 2020 August 1. The other is epoch 3.1 on 2023 February 4, which was taken ∼1 yr after the peak of the previous flare. We retrieve tables and cutouts from the VLASS quick-look catalog from CIRADA[17] and confirm that no source has been detected within a radius of 1′ in all three epochs. Hence, we shall not discuss the radio properties in this work.

Appendix B
Fitting Plots for Optical Spectra

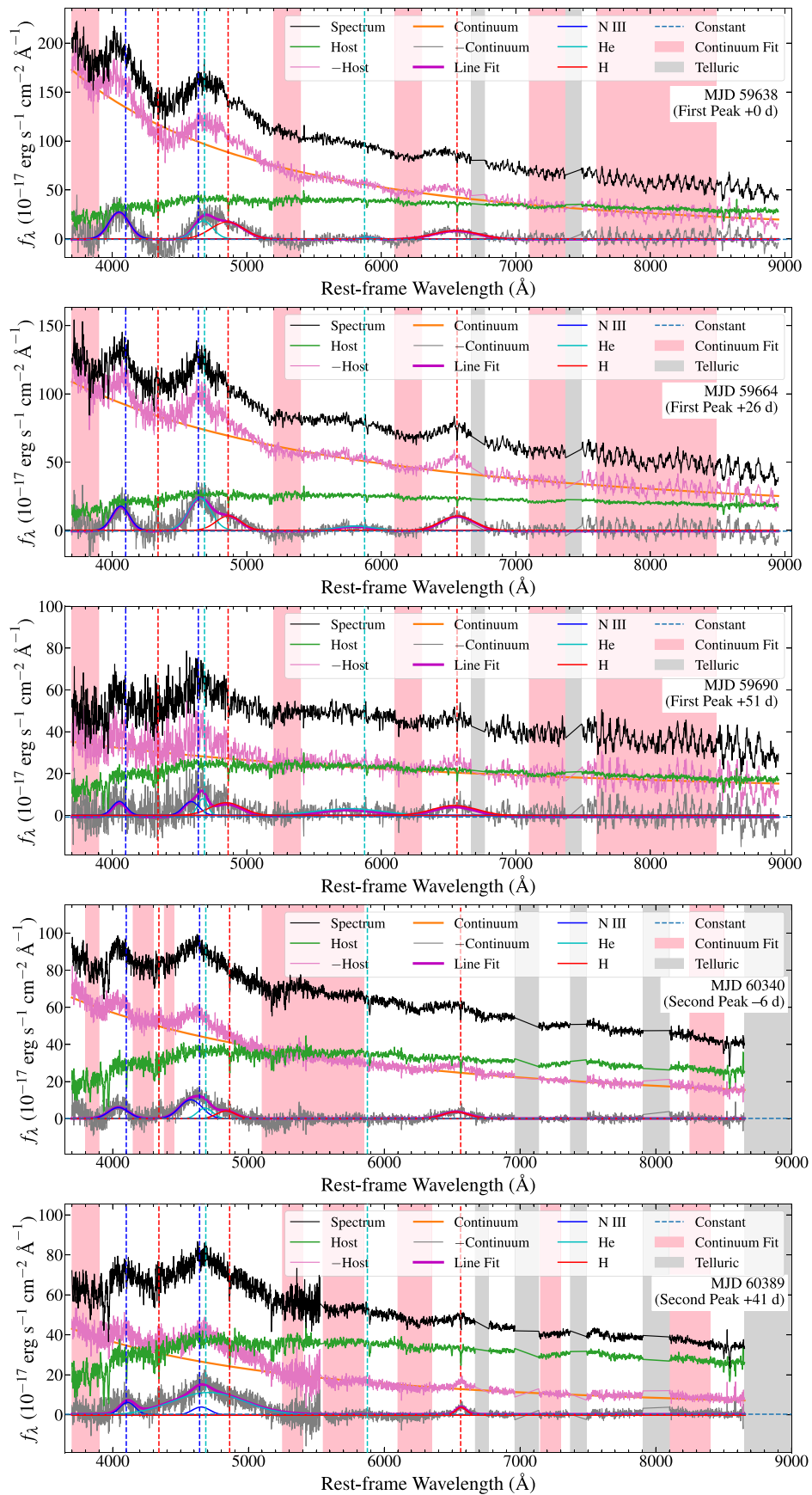In Figure B1, we plot the fitting results for optical spectra individually.

16 https://www.wis-tns.org/astronotes/astronote/2022-57

17 https://cirada.ca/vlasscatalogueql0

12

Figure B1. The fitting plots for optical spectra of AT 2022dbl.

ORCID iDs

Zheyu Lin https://orcid.org/0000-0003-4959-1625
Ning Jiang https://orcid.org/0000-0002-7152-3621
Tinggui Wang https://orcid.org/0000-0002-1517-6792
Xu Kong https://orcid.org/0000-0002-7660-2273
Dongyue Li https://orcid.org/0000-0002-4562-7179
Han He https://orcid.org/0009-0007-7292-8392
Yibo Wang https://orcid.org/0000-0003-4225-5442
Jiazheng Zhu https://orcid.org/0000-0003-3824-9496
Wentao Li https://orcid.org/0009-0006-2521-033X
Ji-an Jiang https://orcid.org/0000-0002-9092-0593
Avinash Singh https://orcid.org/0000-0003-2091-622X
Rishabh Singh Teja https://orcid.org/0000-0002-0525-0872
D. K. Sahu https://orcid.org/0000-0002-6688-0800
Chichuan Jin https://orcid.org/0000-0002-2006-1615
Keiichi Maeda https://orcid.org/0000-0003-2611-7269
Shifeng Huang https://orcid.org/0000-0001-7689-6382

References

Ahumada, R., Allende Prieto, C., Almeida, A., et al. 2020, ApJS, 249, 3
Arcavi, I., Gal-Yam, A., Sullivan, M., et al. 2014, ApJ, 793, 38
Bade, N., Komossa, S., & Dahlem, M. 1996, A&A, 309, L35
Bandopadhyay, A., Coughlin, E. R., Nixon, C. J., & Pasham, D. R. 2024, arXiv:2406.03675
Becker, A., 2015 HOTPANTS: High Order Transform of PSF ANd Template Subtraction, Astrophysics Source Code Library, ascl:1504.004
Bortolas, E. 2022, MNRAS, 511, 2885
Brown, T. M., Baliber, N., Bianco, F. B., et al. 2013, PASP, 125, 1031
Burrows, D. N., Hill, J. E., Nousek, J. A., et al. 2005, SSRv, 120, 165
Campana, S., Mainetti, D., Colpi, M., et al. 2015, A&A, 581, A17
Cannizzo, J. K., Lee, H. M., & Goodman, J. 1990, ApJ, 351, 38
Cappellari, M. 2023, MNRAS, 526, 3273
Charalampopoulos, P., Leloudas, G., Malesani, D. B., et al. 2022, A&A, 659, A34
Chen, J.-H., & Shen, R.-F. 2021, ApJ, 914, 69
Conroy, C., Gunn, J. E., & White, M. 2009, ApJ, 699, 486
Cufari, M., Coughlin, E. R., & Nixon, C. J. 2022, ApJL, 929, L20
Cutri, R. M., Wright, E. L., Conrow, T., et al. 2021, VizieR On-line Data Catalog, II/328
Dai, L., McKinney, J. C., Roth, N., Ramirez-Ruiz, E., & Miller, M. C. 2018, ApJL, 859, L20
Drake, A. J., Djorgovski, S. G., Mahabal, A., et al. 2009, ApJ, 696, 870
Esquej, P., Saxton, R. D., Freyberg, M. J., et al. 2007, A&A, 462, L49
Evans, P. A., Beardmore, A. P., Page, K. L., et al. 2007, A&A, 469, 379
Evans, P. A., Beardmore, A. P., Page, K. L., et al. 2009, MNRAS, 397, 1177
Evans, P. A., Nixon, C. J., Campana, S., et al. 2023, NatAs, 7, 1368
Fitzpatrick, E. L. 1999, PASP, 111, 63
Flewelling, H. A., Magnier, E. A., Chambers, K. C., et al. 2020, ApJS, 251, 7
French, K. D., Arcavi, I., & Zabludoff, A. 2016, ApJL, 818, L21
Gezari, S. 2021, ARA&A, 59, 21
Grupe, D., Beuermann, K., Mannheim, K., et al. 1995, A&A, 299, L5
Grupe, D., Komossa, S., & Saxton, R. 2015, ApJL, 803, L28
Grupe, D., Komossa, S., & Wolsing, S. 2024, ApJ, 969, 98
Guillochon, J., & Ramirez-Ruiz, E. 2013, ApJ, 767, 25
Guolo, M., Gezari, S., Yao, Y., et al. 2024a, ApJ, 966, 160
Guolo, M., Pasham, D. R., Zajaček, M., et al. 2024b, NatAs, 8, 347
Hammerstein, E., Gezari, S., van Velzen, S., et al. 2021, ApJL, 908, L20
Hammerstein, E., van Velzen, S., Gezari, S., et al. 2023, ApJ, 942, 9
Hampel, J., Komossa, S., Greiner, J., et al. 2022, RAA, 22, 055004
HI4PI Collaboration, Ben Bekhti, N., Flöer, L., et al. 2016, A&A, 594, A116
Hills, J. G. 1975, Natur, 254, 295
Hills, J. G. 1988, Natur, 331, 687
Huang, S., Jiang, N., Shen, R.-F., Wang, T., & Sheng, Z. 2023, ApJL, 956, L46
Ivezić, Ž., Kahn, S. M., Tyson, J. A., et al. 2019, ApJ, 873, 111
Jayasinghe, T., Kochanek, C. S., Stanek, K. Z., et al. 2018, MNRAS, 477, 3145
Jiang, N., Dou, L., Wang, T., et al. 2016, ApJL, 828, L14
Jiang, N., Wang, T., Hu, X., et al. 2021, ApJ, 911, 31
Johnson, B. D., Leja, J., Conroy, C., & Speagle, J. S. 2021, ApJS, 254, 22
Kochanek, C. S., Shappee, B. J., Stanek, K. Z., et al. 2017, PASP, 129, 104502
Komossa, S., & Bade, N. 1999, A&A, 343, 775

König, O., Saxton, R. D., Kretschmar, P., et al. 2022, A&C, 38, 100529
Kormendy, J., & Ho, L. C. 2013, ARA&A, 51, 511
Kraft, R. P., Burrows, D. N., & Nousek, J. A. 1991, ApJ, 374, 344
Lacy, M., Baum, S. A., Chandler, C. J., et al. 2020, PASP, 132, 035001
Law-Smith, J., MacLeod, M., Guillochon, J., Macias, P., & Ramirez-Ruiz, E. 2017, ApJ, 841, 132
Leloudas, G., Dai, L., Arcavi, I., et al. 2019, ApJ, 887, 218
Lin, Z., Jiang, N., & Kong, X. 2022, MNRAS, 513, 2422
Liu, C., Yarza, R., & Ramirez-Ruiz, E. 2024, arXiv:2406.01670
Liu, F. K., Cao, C. Y., Abramowicz, M. A., et al. 2021, ApJ, 908, 179
Liu, Z., Malyali, A., Krumpe, M., et al. 2023, A&A, 669, A75
Liu, Z., Ryu, T., Goodwin, A. J., et al. 2024, A&A, 683, 13
Loeb, A., & Ulmer, A. 1997, ApJ, 489, 573
Lu, W., & Bonnerot, C. 2020, MNRAS, 492, 686
Lu, W., & Kumar, P. 2018, ApJ, 865, 128
Lu, W., & Quataert, E. 2023, MNRAS, 524, 6247
Mainzer, A., Bauer, J., Grav, T., et al. 2011, ApJ, 731, 53
Mainzer, A., Bauer, J., Cutri, R. M., et al. 2014, ApJ, 792, 30
Malyali, A., Liu, Z., Rau, A., et al. 2023, MNRAS, 520, 3549
Mandel, I., & Levin, Y. 2015, ApJL, 805, L4
Martin, D. C., Fanson, J., Schiminovich, D., et al. 2005, ApJL, 619, L1
Masci, F. J., Laher, R. R., Rusholme, B., et al. 2019, PASP, 131, 018003
Metzger, B. D., & Stone, N. C. 2016, MNRAS, 461, 948
Nicholl, M. 2018, RNAAS, 2, 230
Oke, J. B. 1974, ApJS, 27, 21
Oke, J. B., & Gunn, J. E. 1982, PASP, 94, 586
Osterbrock, D. E., & Ferland, G. J. 2006, Astrophysics of Gaseous Nebulae and Active Galactic Nuclei (Melville, NY: Univ. Science Books)
Pasham, D., Coughlin, E., Guolo, M., et al. 2024, arXiv:2406.18124
Payne, A. V., Auchettl, K., Shappee, B. J., et al. 2023, ApJ, 951, 134
Payne, A. V., Shappee, B. J., Hinkle, J. T., et al. 2021, ApJ, 910, 125
Payne, A. V., Shappee, B. J., Hinkle, J. T., et al. 2022, ApJ, 926, 142
Pfister, H., Volonteri, M., Dai, J. L., & Colpi, M. 2020, MNRAS, 497, 2276
Piran, T., Svirski, G., Krolik, J., Cheng, R. M., & Shiokawa, H. 2015, ApJ, 806, 164
Planck Collaboration, Aghanim, N., Ashdown, M., et al. 2016, A&A, 596, A109
Prabhu, T. P. 2014, PINSA, 80, 887
Prochaska, J., Hennawi, J., Westfall, K., et al. 2020, JOSS, 5, 2308
Rees, M. J. 1988, Natur, 333, 523
Rees, M. J. 1990, Sci, 247, 817
Reines, A. E., & Volonteri, M. 2015, ApJ, 813, 82
Roming, P. W. A., Kennedy, T. E., Mason, K. O., et al. 2005, SSRv, 120, 95
Ryu, T., Krolik, J., Piran, T., & Noble, S. C. 2020a, ApJ, 904, 99
Ryu, T., Krolik, J., Piran, T., & Noble, S. C. 2020b, ApJ, 904, 101
Sfaradi, I., Horesh, A., & Fender, R. 2022, TNSAN, 57, 1
Shappee, B. J., Prieto, J. L., Grupe, D., et al. 2014, ApJ, 788, 48
Shingles, L., Smith, K. W., Young, D. R., et al. 2021, TNSAN, 7, 1
Singh, A., 2021 RedPipe: Reduction Pipeline, Astrophysics Source Code Library, ascl:2106.024
Skrutskie, M. F., Cutri, R. M., Stiening, R., et al. 2006, AJ, 131, 1163
Smith, K. W., Smartt, S. J., Young, D. R., et al. 2020, PASP, 132, 085002
Somalwar, J. J., Ravi, V., & Lu, W. 2023a, arXiv:2310.03795
Somalwar, J. J., Ravi, V., Yao, Y., et al. 2023b, arXiv:2310.03782
Speagle, J. S. 2020, MNRAS, 493, 3132
Stern, D., Assef, R. J., Benford, D. J., et al. 2012, ApJ, 753, 30
Stone, N. C., & Metzger, B. D. 2016, MNRAS, 455, 859
Stone, N. C., Vasiliev, E., Kesden, M., et al. 2020, SSRv, 216, 35
Teboul, O., Stone, N. C., & Ostriker, J. P. 2024, MNRAS, 527, 3094
Thomsen, L. L., Kwan, T. M., Dai, L., et al. 2022, ApJL, 937, L28
Tonry, J. L., Denneau, L., Heinze, A. N., et al. 2018, PASP, 130, 064505
Ulmer, A. 1999, ApJ, 514, 180
van Velzen, S., Holoien, T. W. S., Onori, F., Hung, T., & Arcavi, I. 2020, SSRv, 216, 124
van Velzen, S., Mendez, A. J., Krolik, J. H., & Gorjian, V. 2016, ApJ, 829, 19
Wang, J., & Merritt, D. 2004, ApJ, 600, 149
Wang, M., Ma, Y., Wu, Q., & Jiang, N. 2024, ApJ, 960, 69
Wang, T., Liu, G., Cai, Z., et al. 2023, SCPMA, 66, 109512
Wevers, T., Coughlin, E. R., Pasham, D. R., et al. 2023, ApJL, 942, L33
Wevers, T., Pasham, D. R., van Velzen, S., et al. 2019, MNRAS, 488, 4816
Wright, E. L., Eisenhardt, P. R. M., Mainzer, A. K., et al. 2010, AJ, 140, 1868
Wu, X.-J., & Yuan, Y.-F. 2018, MNRAS, 479, 1569
Yao, Y., Ravi, V., Gezari, S., et al. 2023, ApJL, 955, L6
Zhong, S., Li, S., Berczik, P., & Spurzem, R. 2022, ApJ, 933, 96
Zhu, J., Jiang, N., Wang, T., et al. 2023, ApJL, 952, L35